PLANETARY SCIENCE

Krypton isotopes and noble gas abundances in the coma of comet 67P/Churyumov-Gerasimenko

Martin Rubin[1]*, Kathrin Altwegg[1,2], Hans Balsiger[1], Akiva Bar-Nun[3†], Jean-Jacques Berthelier[4], Christelle Briois[5], Ursina Calmonte[1], Michael Combi[6], Johan De Keyser[7], Björn Fiethe[8], Stephen A. Fuselier[9,10], Sebastien Gasc[1], Tamas I. Gombosi[6], Kenneth C. Hansen[6], Ernest Kopp[1], Axel Korth[11], Diana Laufer[3], Léna Le Roy[1], Urs Mall[11], Bernard Marty[12], Olivier Mousis[13], Tobias Owen[14†], Henri Rème[15,16], Thierry Sémon[1], Chia-Yu Tzou[1], Jack H. Waite[8], Peter Wurz[1,2]

The Rosetta Orbiter Spectrometer for Ion and Neutral Analysis mass spectrometer Double Focusing Mass Spectrometer on board the European Space Agency's Rosetta spacecraft detected the major isotopes of the noble gases argon, krypton, and xenon in the coma of comet 67P/Churyumov-Gerasimenko. Earlier, it was found that xenon exhibits an isotopic composition distinct from anywhere else in the solar system. However, argon isotopes, within error, were shown to be consistent with solar isotope abundances. This discrepancy suggested an additional exotic component of xenon in comet 67P/Churyumov-Gerasimenko. We show that krypton also exhibits an isotopic composition close to solar. Furthermore, we found the argon to krypton and the krypton to xenon ratios in the comet to be lower than solar, which is a necessity to postulate an addition of exotic xenon in the comet.

INTRODUCTION

The European Space Agency's (ESA) Rosetta spacecraft accompanied comet 67P/Churyumov-Gerasimenko (hereafter 67P/C-G) over 2 years (1). In August 2014, the comet moved from a heliocentric distance of more than 3 astronomical units (AU) to perihelion in August 2015 at 1.24 AU and again away from the Sun. The Rosetta Orbiter Spectrometer for Ion and Neutral Analysis (ROSINA) monitored the abundances of volatiles in the coma of the comet in situ at the location of the spacecraft (2). The major components in the coma have been shown to be H_2O, CO_2, CO, and O_2 (3, 4), with strong variations depending on the location of the spacecraft with respect to the comet's heliocentric distance and solar illumination angle (5). As the comet approached the Sun, the activity increased and peaked some 2 to 3 weeks after perihelion passage (6). As the environment became increasingly dusty close to perihelion and the Rosetta star trackers encountered problems distinguishing stars from illuminated grains of cometary origin,

the spacecraft was moved to larger cometocentric distances with lower dust abundances.

Volatile species measured in the coma have been released from the nucleus. Previous studies found that most of the ROSINA results could be explained without having to invoke significant contributions from distributed sources (6, 7). However, the changing illumination conditions and hence temperatures on the surface and the strong dichotomy of the northern and southern hemispheres of the nucleus, which hints at different processing of the surface (8, 9), make it difficult to derive ratios of the bulk volatile composition inside the nucleus. These relative abundances, however, are crucial to study the composition of the nascent solar system and the physical conditions under which it formed.

Early in the mission, Rosetta spent an extended amount of time close to the nucleus. In October 2014, at a 10-km distance from the nucleus, ROSINA detected ^{36}Ar and ^{38}Ar, the two stable primordial noble gas isotopes of argon, respectively (10). The $^{36}Ar/^{38}Ar$ ratio was measured to be 5.4 ± 1.4, and this ratio is in agreement with the solar abundance ratio of 5.37 (11) within (large) errors. The ROSINA observations also revealed a remarkable correlation of argon with molecular nitrogen, N_2, of $^{36}Ar/N_2 = (9.1 ± 0.3) × 10^{-3}$, while the ratio with respect to H_2O showed a much larger variation of $^{36}Ar/H_2O = (0.1 \text{ to } 2.3) × 10^{-5}$. These measurements were obtained far from perihelion at a distance of 3.1 AU. Late in the mission, in May 2016 when Rosetta was close to the nucleus of the comet, xenon was also detected. The seven major stable xenon isotopes (^{128}Xe, ^{129}Xe, ^{130}Xe, ^{131}Xe, ^{132}Xe, ^{134}Xe, and ^{136}Xe) found in the coma of 67P/C-G (12) showed an isotopic composition remarkably different from solar (12, 13). The heavy isotopes, ^{134}Xe and ^{136}Xe, were depleted, while, on the other hand, ^{129}Xe showed enrichment with respect to solar and to chondritic values. Two possible causes were discussed (12): on the one hand, an r-process isotope deficiency relative to solar (or excess of s-process isotopes, which is equivalent) with an additional source for ^{129}Xe [possibly from the decay of now extinct ^{129}I with a half-life of 15.7 million years (Ma)] and on the other hand, a mass-dependent fractionation, which was then deemed improbable given the 67P/C-G xenon isotopic pattern. The accuracy of the measurements, however, did not allow for an unambiguous identification of the details of the underlying processes. Remarkably, 67P-C-G xenon

[1]Physikalisches Institut, University of Bern, Sidlerstrasse 5, CH-3012 Bern, Switzerland. [2]Center for Space and Habitability, University of Bern, Gesellschaftsstrasse 6, CH-3012 Bern, Switzerland. [3]Department of Geophysics, Tel Aviv University, Ramat-Aviv, Tel Aviv, Israel. [4]Laboratoire Atmosphères, Milieux, Observations Spatiales, Institut Pierre Simon Laplace, CNRS, Université Pierre et Marie Curie, 4 Place Jussieu, 75252 Paris Cedex 05, France. [5]Laboratoire de Physique et Chimie de l'Environnement et de l'Espace, UMR 6115 CNRS–Université d'Orléans, Orléans, France. [6]Department of Climate and Space Sciences and Engineering, University of Michigan, 2455 Hayward, Ann Arbor, MI 48109, USA. [7]Koninklijk Belgisch Instituut voor Ruimte-Aeronomie–Institut Royal Belge d'Aéronomie Spatiale, Ringlaan 3, B-1180 Brussels, Belgium. [8]Institute of Computer and Network Engineering, Technische Universität Braunschweig, Hans-Sommer-Straße 66, D-38106 Braunschweig, Germany. [9]Space Science Directorate, Southwest Research Institute, 6220 Culebra Road, San Antonio, TX 78228, USA. [10]University of Texas at San Antonio, San Antonio, TX 78249, USA. [11]Max-Planck-Institut für Sonnensystemforschung, Justus-von-Liebig-Weg 3, 37077 Göttingen, Germany. [12]Centre de Recherches Pétrographiques et Géochimiques, CNRS, Université de Lorraine, 15 rue Notre Dame des Pauvres, BP 20, 54501 Vandoeuvre lès Nancy, France. [13]Laboratoire d'Astrophysique de Marseille, CNRS, Aix-Marseille Université, 13388 Marseille, France. [14]Institute for Astronomy, University of Hawaii, Honolulu, HI 96822, USA. [15]Institut de Recherche en Astrophysique et Planétologie, CNRS, Université Paul Sabatier, Observatoire Midi-Pyrénées, 9 Avenue du Colonel Roche, 31028 Toulouse Cedex 4, France. [16]Centre National d'Études Spatiales, 2 Place Maurice Quentin, 75001 Paris, France.
*Corresponding author. Email: martin.rubin@space.unibe.ch
†Deceased.

fitted the ^{134}Xe-^{136}Xe depletion well (relative to solar or chondritic) required to make the ancestor of terrestrial xenon (labeled Xe-U) and permitted to estimate the proportion of cometary xenon in the terrestrial atmosphere (12).

During the same time period late in the Rosetta mission, the isotopes of krypton, namely, ^{80}K, ^{82}Kr, ^{83}Kr, ^{84}Kr, and ^{86}Kr, have also been detected. Here, we report on their isotopic ratios and the corresponding relative abundances of the noble gases argon, krypton, and xenon (neon was not detected).

RESULTS

ROSINA Double Focusing Mass Spectrometer

ROSINA consists of the Double Focusing Mass Spectrometer (DFMS), the Reflectron-type Time-Of-Flight (RTOF) mass spectrometer, and the COmet Pressure Sensor (COPS). The two mass spectrometers complement each other with high mass resolution (DFMS) and high time resolution (RTOF). Here, we focus on neutral composition measurements performed by ROSINA DFMS. In neutral mode, particles are first ionized through electron impact and then separated on the basis of their mass-to-charge ratio in an electric and then a magnetic field before hitting the detector. All errors given in this paper are 1-σ. More details about DFMS and the data analysis can be found in Materials and Methods.

DFMS observations in May 2016

In the late portion of the mission, Rosetta spent more time close to the nucleus, and ROSINA detected the noble gas xenon (12). For this purpose, we investigated ROSINA DFMS data obtained between 14 and 31 May 2016 between 10 and 7 km from the nucleus' center of mass. The observations were performed 2 months after the outbound equinox and mostly above the southern hemisphere that remained more active despite the subsolar latitude moving to the northern hemisphere. As the spacecraft was slowly approaching the comet, the DFMS detector count rates slightly increased. Three overlapping time periods were analyzed, as follows: (i) 14 to 31 May 2016, (ii) 20 to 31 May 2016, and (iii) 26 to 31 May 2016. Period (i) contained approximately 500 individual mass spectra but had the lowest average count rates, period (ii) was an average of approximately 260 spectra with medium average count rates and was also contained in period (i), and period (iii) was based on approximately 70 spectra with the highest average count rates and was also part of both periods (i) and (ii). Similar results were obtained for all three periods, and the analysis was focused on period (ii), which was a compromise of high enough average count rates to investigate the less abundant ^{128}Xe and ^{130}Xe and the number of spectra used in the averaging process.

During the same 2.5 weeks in May 2016, when Rosetta was inside of 15 km from the comet center, ROSINA also detected the isotopes of the noble gas krypton (^{80}Kr, ^{82}Kr, ^{83}Kr, ^{84}Kr, and ^{86}Kr). We performed the data analysis for the same three periods as for xenon. However, on the basis of the higher instrument sensitivity for krypton versus xenon and the resulting higher average count rates, we focused on period (i), which contains the full data set of more than 500 spectra per mass line and includes periods (ii) and (iii). The data analysis was the same as for xenon (12), and details are in Materials and Methods. Figure S1 shows the averages of period (i) of the 500 individual spectra for each isotope (^{82}Kr, ^{83}Kr, ^{84}Kr, and ^{86}Kr), and Fig. 1 shows the isotopic ratios normalized to ^{84}Kr and to the solar wind (SW) composition (discussion follows later). The mass spectra in fig. S1 also show fragments of hexane, C_6H_{14}, and higher-mass organic species, which shall be discussed elsewhere.

The ^{80}Kr mass line has a strong interference with carbon disulfide with two heavy sulfur isotopes, $C^{34}S_2$. The resulting large error bars for ^{80}Kr did not allow a meaningful contribution to our analysis, and thus, we also omitted the corresponding spectra from the figure. ^{78}Kr is unfortunately fully hidden below carbon disulfide containing one heavy sulfur isotope, $C^{34}S^{32}S$, and therefore excluded from our analysis. Table S1 shows the corresponding results for the three periods (i) to (iii). The counts represent the sum of counts under the peak (sum of the red points in fig. S1) averaged per isotope with the statistical count, offset, and fit errors indicated below.

The noble gas measurements in May 2016 were performed above the southern hemisphere during ever-closer orbits in the terminator plane as the comet rotated once per approximately 12 hours. Still, at these distances, the whole comet was in the field of view of DFMS, and gas may have come from any location on the nucleus facing Rosetta. During the 2.5 weeks of observations, the heliocentric distance of the comet increased only slightly. These small changes and the fact that there was no spacecraft slewing (that could change the background) thus provided stable observation conditions throughout the period chosen. Figure S2 shows Rosetta's position with respect to the comet for the time of observation and the three investigated time intervals.

Relative noble gas abundances from May 2016

In all three periods, the noble gas argon has been also detected. By combining these observations, the relative abundances of the ^{36}Ar, ^{84}Kr, and ^{132}Xe noble gas isotopes are obtained. Figure 2A shows the abundances of ^{84}Kr versus ^{36}Ar. Because of the low count rates for krypton, daily averages are plotted, with the day of the month indicated next to the measurement. Figure 2 shows a reasonable correlation between ^{36}Ar and ^{84}Kr. The interference of ^{36}Ar with $H^{35}Cl$ and $H_2^{34}S$ (10, 14, 15) leads to larger error bars compared to the well-separated ^{84}Kr peak. The slope of ^{84}Kr/^{36}Ar = 0.089 ± 0.021 indicates their relative abundance. Figure 2B shows the same features but for ^{132}Xe as a function of ^{84}Kr, which
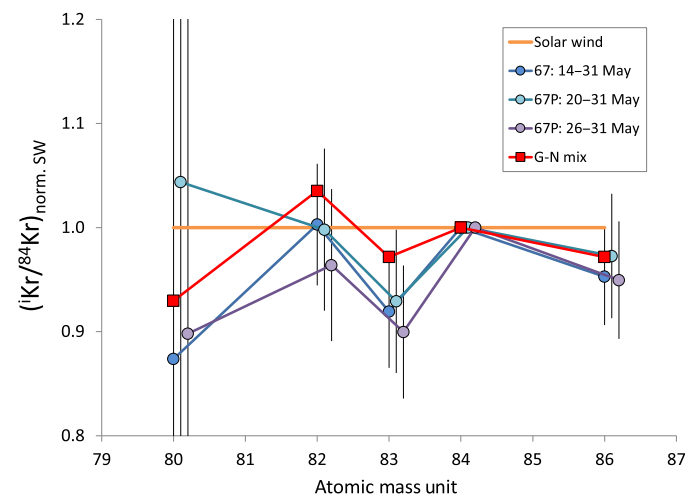

Fig. 1. Isotopic composition of 67P/C-G krypton, normalized to ^{84}Kr and the SW composition [from (18)]. 67P/C-G errors reflect 1-σ SEM and calibration uncertainties for the corresponding averaging periods. In this format, SW-Kr is represented by the horizontal orange line. ^{83}Kr appears to be slightly depleted relative to solar. The red line represents a mix of different nucleosynthetic components [the so-called G-Kr and N-Kr components; (11, 20)]. For the G-Kr composition, we consider the weak s-process composition having low ^{86}Kr/^{84}Kr ratios (20). The best fit was obtained for a proportion of 5% G-Kr in cometary krypton.

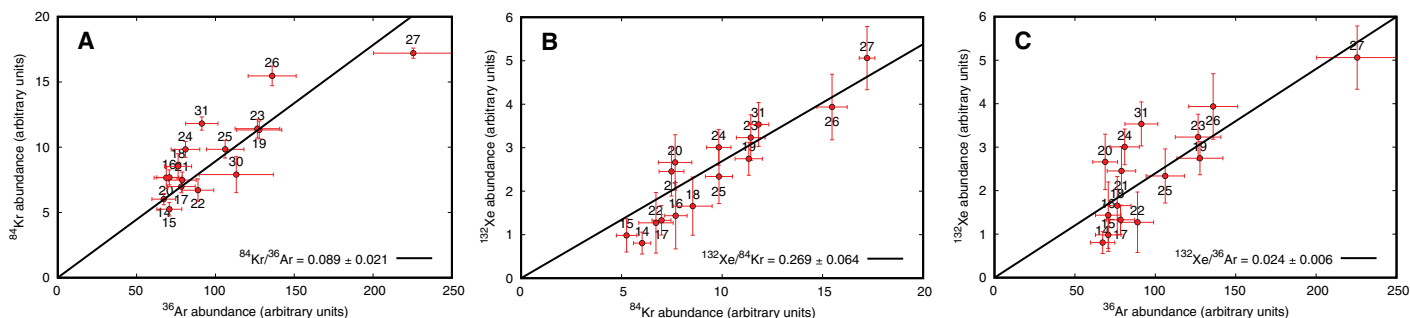**Fig. 2. Relative abundances of the major isotopes of argon, krypton, and xenon.** (**A**) ^{84}Kr versus ^{36}Ar relative abundances obtained from daily averages with SEM error bars for the 14 to 31 May 2016 period ($R^2 = 0.67$). (**B**) ^{132}Xe versus ^{84}Kr. (**C**) ^{132}Xe versus ^{36}Ar. The number associated with each point indicates the day ($R^2 = 0.83$). The error of the daily averages includes the statistical errors, whereas for the slopes, a 16% calibration uncertainty for each element is included. A correlation coefficient of 0.76 was found between the $^{132}Xe/^{36}Ar$ and $^{84}Kr/^{36}Ar$ slopes (A and C).

exhibits a slope of $^{132}Xe/^{84}Kr = 0.269 \pm 0.064$. In addition to errors from counting statistics, the errors of the slopes contain 16% uncertainty of the measured sensitivities of argon, krypton, and xenon obtained in the laboratory calibration campaign (more details in the Supplementary Materials). Not all daily averages contain the same number of spectra, and for 30 May 2016, there were only two spectra, which was not enough to derive a xenon abundance. On 28 and 29 May 2016, no measurements were performed because of an outage of the Rosetta star trackers caused by excessive dust and the ensuing safe mode of the spacecraft. These results correspond to the ratio of the local densities of $^{36}Ar/^{132}Xe = 41.7 \pm 10.1$, $^{36}Ar/^{84}Kr = 11.2 \pm 2.6$, and $^{84}Kr/^{132}Xe = 3.7 \pm 0.9$.

However, these slopes might not reflect the actual relative noble gas production rates of the comet as there is a local enhancement of the density of heavier species due to the lower outgassing velocity. Equal outgassing velocities can only be expected in the dense, collisionally coupled coma. At the location of the spacecraft, the coma of 67P/C-G was always very thin, with very long collisional mean free paths. Numerical simulations based on the Direct Simulation Monte Carlo technique (6, 16) have been carried out through a range of heliocentric distances showing that, beyond 3 AU, the individual species collisionally decouple directly at the surface. We therefore applied a correction factor assuming a $1/\sqrt{mass}$ dependence of the outgassing velocity and the corresponding production rate ratio from the nucleus. This assumption implies the same temperatures of the species in the gas phase after passing the surface dust layer through thermal accommodation by collisions and the same (subsurface) source regions for the different noble gases (and N_2), which is compatible with the observed correlations shown in Fig. 2. We thus obtain for the relative production rate at the surface of the comet $^{36}Ar/^{132}Xe = 79.8 \pm 19.3$, $^{36}Ar/^{84}Kr = 17.1 \pm 3.9$, and $^{84}Kr/^{132}Xe = 4.7 \pm 1.1$. Table 1 provides a collection of the results with and without applied velocity correction factors. On the other hand, to be able to compare with published argon (10) and xenon (12) data, we have omitted the velocity correction in relative abundances of the detected krypton isotopes that amounts to, for example, 1.2% in the case of $^{86}Kr/^{84}Kr$, which is well within the reported 1-σ error of 4.9% (Fig. 1).

Noble gas bulk abundances in the nucleus of 67P/C-G
We undertook an attempt to derive noble gas bulk abundances relative to water inside the nucleus. Briefly, through molecular nitrogen, N_2, we were able to combine measurements obtained late in the mission when Rosetta was close enough to the comet to measure Ar/N_2, Kr/Ar, and Xe/Ar with measurements of N_2/H_2O close to perihelion, which better

Table 1. Relative ^{36}Ar, ^{84}Kr, and ^{132}Xe abundances for the 14 to 31 May 2016 period based on approximately 500 spectra. The second column gives the density ratios measured at the location of Rosetta, which are equivalent to the comet's production rate, assuming equal outgassing velocities applicable in a collisional coma. The last column (underlined) represents our best estimate for the bulk abundance where the ratio X_1/X_2 is multiplied by $\sqrt{m_2/m_1}$ to account for different outgassing velocities based on a thermal expansion approximation. Errors reflect 1-σ SEM and calibration uncertainties.

Isotope	Density ratio at Rosetta	$\sqrt{m_2/m_1}$	Production rate ratio of 67P/C-G
$^{36}Ar/^{132}Xe$	41.7 ± 10.1	1.915	$\underline{79.8 \pm 19.3}$
$^{36}Ar/^{84}Kr$	11.2 ± 2.6	1.527	$\underline{17.1 \pm 3.9}$
$^{84}Kr/^{132}Xe$	3.7 ± 0.9	1.254	$\underline{4.7 \pm 1.1}$

reflect bulk abundances inside the nucleus but were obtained too far from the comet to measure noble gases. The results listed in Table 2 were limited to the southern hemisphere, which was responsible for the major fraction of the total outgassing during that time (17) and where fresh material is therefore exposed during each pericenter passage (9). Any species and temperature dependence in the sublimation process would have to be considered on top of the numbers presented in this paper (apart from the velocity correction).

The first assumption is that noble gases are released in proportion to their relative abundances in the comet's nucleus. Relative abundances of ^{36}Ar, ^{84}Kr, and ^{132}Xe are presented in the previous section. Furthermore, we derived the fraction of ^{36}Ar isotopes with respect to the total amount of argon of 0.844 ± 0.034 (10). The same can be obtained for $^{84}Kr/Kr = 0.582 \pm 0.010$ (this work) and $^{132}Xe/Xe = 0.253 \pm 0.012$ (12), respectively (see also table S2).

Given the increased activity and hence the dusty near-nucleus environment, the Rosetta spacecraft was moved to larger cometocentric distances. Therefore, ROSINA could not detect the noble gases during the most active period of the comet. Inspired by earlier observations (10), we again investigated molecular nitrogen, N_2, which was abundant enough to be observed throughout the mission. While measured above the southern hemisphere this time, N_2 and ^{36}Ar still show a strong correlation. Figure 3B shows the correlation between N_2 and ^{36}Ar for

Table 2. Best-estimate bulk abundances of noble gases in comet 67P/C-G in the second column. The third column gives the correction factor applied to the values from the second column in table S3 based on the expected outgassing velocities. We assume that, close to perihelion, N_2 and H_2O share the same velocity due to collisional coupling and apply no correction. Hence, for the May 2016 period, the reference mass for the $1/\sqrt{m}$ velocity correction becomes that of molecular nitrogen (m_1 = 28 u) instead of water (18 u). Errors reflect 1-σ SEM and calibration uncertainties.

Species	Production rate ratio of 67P/C-G	$\sqrt{m_2/m_1}$	Conditions/notes
N_2/H_2O	$(8.9 \pm 2.4) \times 10^{-4}$	(1.000)	Collisional, measured near perihelion
$^{36}Ar/N_2$	$(5.5 \pm 1.5) \times 10^{-3}$	0.882	Rarefied, measured beyond 3 AU
$^{36}A/H_2O$	$(4.9 \pm 1.9) \times 10^{-6}$	0.882	Combination of rarefied and collisional
Ar/H_2O	$(5.8 \pm 2.2) \times 10^{-6}$	0.882·(1.000)	Combination of rarefied and collisional
Kr/H_2O	$(4.9 \pm 2.2) \times 10^{-7}$	0.577	Combination of rarefied and collisional
Xe/H_2O	$(2.4 \pm 1.1) \times 10^{-7}$	0.461	Combination of rarefied and collisional
Ne/H_2O	$<5 \times 10^{-8}$	1.128	Upper limit
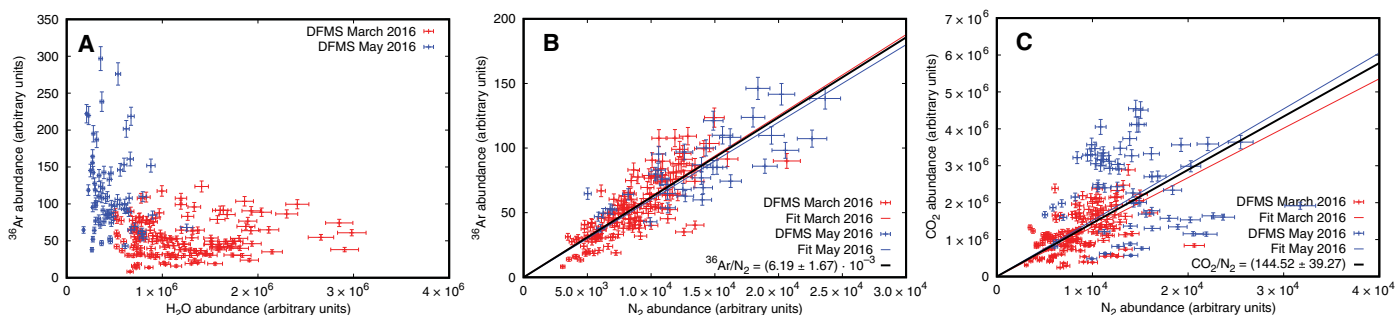
Fig. 3. Relative abundances of ^{36}Ar, N_2, and CO_2. ^{36}Ar to H_2O abundances for 9 to 21 March 2016 (red) and 14 to 31 May 2016 (blue) in (**A**), ^{36}Ar to N_2 abundances in (**B**), and N_2 to CO_2 in (**C**). The individual measurements show statistical errors. The error of the slope for the combined measurements (black) includes the statistical error, 18% calibration uncertainty (sensitivity and fragmentation pattern for each species), and 20% gain error ($R^2 = 0.70$ for $^{36}Ar/N_2$ and $R^2 = 0.12$ for CO_2/N_2).

period (i) and 2 months earlier during 9 to 21 March 2016 when the spacecraft was sufficiently close to the nucleus for the detection of argon. Figure 3C shows N_2 (and hence ^{36}Ar) versus CO_2 and ^{36}Ar versus H_2O (Fig. 3A). Both sets of measurements from May 2016 and March 2016 were obtained at different cometocentric distances, and hence, the local densities of ^{36}Ar at the spacecraft were higher for the period in May despite the larger heliocentric distance. The illumination of the nucleus also changed as the outbound equinox in March 2016 marked the start of summer in the northern hemisphere. The water production again followed the subsolar latitude to the northern hemisphere (17), while noble gases were still more dominant above the southern hemisphere. For these reasons, a marked change in the $^{36}Ar/H_2O$ ratio can be observed, while $^{36}Ar/N_2$ remains well correlated. The slope of $^{36}Ar/N_2$ of ~6.2 × 10^{-3} is somewhat less steep compared to the 9.1 × 10^{-3} measured early in the mission (10) above the northern hemisphere, which showed lower relative abundances of highly volatile species (5), possibly due to the redeposition of wet dust (8). We will therefore base our results on the relative abundance of $^{36}Ar/N_2$ of ~6.2 × 10^{-3} measured above the freshly processed southern hemisphere and assume that Ar/N_2 remains more or less unchanged throughout the cometary orbit.

In the next step, the period from May 2015 to early June 2015 was analyzed to estimate bulk abundances in the comet (14). Later on, around perihelion in August 2015, the coma was much more dynamic

with frequent outbursts, which can potentially lead to an overestimation of the highly volatile species (such as N_2) with respect to their bulk abundance. Furthermore, a dedicated Philae lander search required a position above the lesser active northern hemisphere. After perihelion, Rosetta went to even larger distances for an excursion to the bow shock to study the interaction of the comet with the SW. Especially in May 2015, Rosetta not only flew over the active southern hemisphere at negative latitudes but also spent time on the dayside of the comet (phase angles down to 60°) for which we derived a bulk abundance ratio of N_2/H_2O = $(8.9 \pm 2.4) \times 10^{-4}$ (compare Table 2). Details on Rosetta's trajectory before perihelion for May 2015 to early June 2015 can be found in fig. S3. All measurements are restricted to the dayside of the comet (phase angle < 85°) above the southern summer hemisphere (subspacecraft latitude < 0°). Out of this selection, two subsets were analyzed: first, the period of 10 to 31 May 2015, and second, the full month of May and early June (period denoted by the two gray bars in fig. S3). Both periods resulted in very similar N_2/H_2O ratios of ~$(8.9 \pm 2.4) \times 10^{-4}$, which we then adopted for the bulk abundance of N_2. Figure S4 shows the measured N_2/H_2O abundance ratios and the corresponding fits.

Connecting these observations (for example, $^{36}Ar/Ar$, $^{36}Ar/N_2$, and N_2/H_2O) yields an estimation of the bulk abundances of the noble gas argon in comet 67P/C-G with respect to water. Then, including $^{84}Kr/Kr$, $^{132}Xe/Xe$, $^{36}Ar/^{84}Kr$, and $^{36}Ar/^{132}Xe$, we obtained the Kr/H_2O and Xe/H_2O ratios, respectively. The results are summarized in table S3, again

derived directly from the local densities at Rosetta and corrected for different outgassing velocities. The former is applicable for a collisionally coupled coma, while the latter is applicable for a rarefied coma. Although the coma is no longer collisional at a few 100 km, where Rosetta was located in May 2015 and June 2015, it is likely that N_2 and H_2O have similar outgassing velocities due to collisional coupling within the first few kilometers from the nucleus (16). Therefore, our best estimate in Table 2 assumes collisionally coupled N_2 and H_2O close to the nucleus near perihelion and decoupled velocities for all measurements obtained in the May 2016 period beyond 3 AU.

Throughout the reported measurement period in May 2016, we also looked for the noble gas neon. The lack of a signal of ^{20}Ne on mass/charge 20 u/e and of ^{22}Ne on 22 u/e allows us to derive an upper limit for the neon relative abundance with respect to H_2O of $^{21,22}Ne/H_2O \leq 5 \times 10^{-8}$. The rather low sensitivity of DFMS for neon and thus high upper limit are a consequence of its small cross section for electron impact ionization.

DISCUSSION
Constraints on the origin of cometary ice from the noble gas isotopic composition

The argon isotopic composition of 67P/C-G's coma [$^{36}Ar/^{38}Ar = 5.4 \pm 1.4$; (10)] is not precise enough to distinguish between most solar system reservoirs including meteoritic [the so-called Q component, $^{36}Ar/^{38}Ar = 5.34$; see (11) and references therein] and solar [$^{36}Ar/^{38}Ar = 5.37$ (11)]. Given the error on the 67P/C-G measurement, the argon isotopic composition cannot be distinguished from nucleosynthetic components identified in meteoritic presolar grains, such as P3-Ar (5.26), N-Ar (5.87), or HL-Ar (4.41) [see (11) and references therein]. The isotopic composition of 67P/C-G–Xe is, however, not consistent with a solar-like origin, being depleted in the heavy xenon isotopes (^{134}Xe and ^{136}Xe) and being rich in ^{129}Xe relative to solar. This composition has been attributed to a nucleosynthetic mix different from that of the bulk solar system as opposed to be the result of isotopic mass fractionation, suggesting that cometary ice contains interstellar material (12). Thus, the isotopic composition of krypton may further constrain the origin of cometary material.

Figure 1 represents the krypton isotopic composition recorded in the coma of comet 67P/C-G in May 2016, normalized to ^{84}Kr and to the SW composition (18). Within errors, the 67P/C-G-Kr composition is close to that of the SW, with the possible exception of a deficit in ^{83}Kr. This similarity contrasts with the case of xenon in 67P/C-G, whose isotopic composition is clearly different from solar (12). The large excess in ^{129}Xe was tentatively attributed to the decay of extinct ^{129}I ($T_{1/2} = 16$ Ma), provided that the initial iodine abundance in the parent reservoir of xenon was orders of magnitude higher than that present in meteorites at the beginning of solar system formation, thus implying a presolar origin for the parent xenon reservoir. The deficits of ^{134}Xe and ^{136}Xe could not originate from nuclear processes other than nucleosynthetic ones, and it was suggested that these deficits resulted from a mix of presolar components different from that of the bulk solar system (12). Adopting the nucleosynthetic end-members from correlations in presolar materials (19), Marty et al. argued (12) that the 67P/C-G xenon composition could be reproduced by mixing up an s-process xenon component with two r-process xenon components identified earlier (19).

In principle, a similar mix should be able to reproduce the krypton isotopic composition of the comet. Unfortunately, such an approach is not applicable to krypton because there are no r-process–only isotopes

for krypton (20), and therefore, the identification of pure r-composition(s) cannot be achieved. Thus, the mixing approach done for xenon cannot be applied directly to krypton. The lack of r-process–only krypton isotopes may also explain why the krypton isotopic composition is less variable than that of xenon among solar system reservoirs and objects. Another complication is that the production rates of s-process krypton isotopes in asymptotic giant branch (AGB) stars can vary depending on the stellar regime. This is because ^{86}Kr (and ^{80}Kr) is affected by branching in the s-process, contrary to $^{82,83,84}Kr$ isotopes. The abundances of ^{86}Kr and ^{80}Kr have been found to be variable among SiC grains (20), in proportions that are consistent with theoretical models [for example, (21)].

It has been observed (20) that the krypton isotopic ratios of SiC grains define good mixing correlations between two nucleosynthetic end-members identified as an s-process component labeled G-Kr and a "normal" component labeled N-Kr. The normal composition integrated the contribution of several nucleosynthetic sources and could represent the nucleosynthetic ancestor of solar system krypton. Later on, a qualitatively similar scenario was proposed (22) to derive the xenon and krypton isotopic compositions of meteorites. An exotic, weak s-process–rich material was added before solar system formation to an ancestral presolar component (labeled "P3") resembling the solar composition. We assume that the krypton isotopic composition of 67P/C-G is the result of the contribution of an exotic component, s-process (G) krypton to normal (N) krypton (20), as observed in SiC grains [end-member data summarized in (11)]. Based on this assumption, the 67P/C-G krypton composition, including the slight deficit in ^{83}Kr, can be reproduced within errors by adding ~5% of the G (s-process) component to the N component (Fig. 1). Taking SW krypton instead of N-Kr would give comparable results because N-Kr is isotopically close to SW-Kr. The data are best fitted by assuming a weak s-process component having a low $^{86}Kr/^{84}Kr$ ratio corresponding to low neutron flux in AGB envelopes (Fig. 1).

If this scenario is correct, then the contribution of s-process material before solar system formation must have also affected the xenon isotopic composition by increasing the s-process contribution relative to the r-process one, which is effectively what is required for 67P/C-G xenon (12). In the Supplementary Materials, we have modeled the compositions of krypton and xenon by assuming a similar mixing scenario for both noble gases. To a normal composition, represented by N-Kr and N-Xe [(11) for end-member compositions] an exotic component (X-Kr and X-Xe, rich in s-process isotopes) is added. For X-Kr, it is not possible to define the r-process contribution for the reason given above, and we use G-Kr (20, 22). For xenon, we use a similar mix of s-process and r-process components reproducing the cometary xenon composition (12). The proportions of the mix that best fit xenon data are 35% s-process xenon and 65% r-process xenon (the latter being the mean of the two r-process end-members (19)). For the s-process xenon component, taking either the composition identified by (19) or the G-Xe composition gives similar results. For the sake of consistency with krypton, we select G-Xe. The best fit for the 67P/C-G composition is obtained for X-Xe = 80% and N-Xe = 20%.

The much higher proportion of the excess component added to xenon (80%) compared to that added to krypton (5%) implies that the $(Xe/Kr)_X$ ratio of the exotic component has to be higher than the $(Xe/Kr)_N$ ratio of the normal (N) component. For the sake of illustration, we assume below that the N-(Xe/Kr) ratio is similar to the solar ratio. In agreement with this requirement, we note that the Xe/Kr ratio of the comet is 4.7 ± 1.8 times the solar ratio [from data in Table 1 and

(13)]. We compute that the $(Xe/Kr)_X$ ratio of the exotic component is ~80 times the solar ratio for a proportion of 5% G-Kr (mixing equations and calculations are given in the Supplementary Materials). We can also compute what would be the corresponding fraction of exotic xenon in cometary xenon, which gives 80%, the remaining 20% being N-Xe. This fraction is in agreement with a fraction of 80% exotic xenon required independently to fit best the xenon isotopic data (fig. S5).

The mixing model proposed above is able to provide a satisfactory solution for explaining the contrasted isotopic compositions of krypton and xenon. This scenario is, however, not without problems since it requires the exotic, s–process–rich component in the comet to be significantly enriched in xenon relative to krypton compared to the solar abundance. Studies of presolar material have shown that xenon is commonly enriched relative to krypton in the s-process end-members, often referred as chemical fractionation (20). These enrichments could be related to differences in the behaviors of xenon and krypton during expulsion from stellar envelopes, such as preferential ionization of xenon relative to krypton, and/or selective implantation of xenon into dust. It is unclear whether such chemical fractionation could have played a role in enriching icy grains with AGB-derived noble gases. Selective trapping or retention of xenon during ice-related processes could have also played a role, and experiments involving noble gas trapping and desorption in ice under conditions relevant to the outer solar system are highly needed.

Noble gas abundance of solar system reservoirs

In Fig. 4, the relative abundances of 67P/C-G noble gases (Table 2) are represented in an $^{84}Kr/^{36}Ar$ versus $^{132}Xe/^{36}Ar$ format, together with solar, Earth, Mars (11), and chondritic [Centre de Recherches Pétrographiques et Géochimiques (CRPG), Nancy compilation of Carbonaceous Orgueil (CI) and Carbonaceous Murchison (CM) data] noble gas compositions including upper limits for Titan (23). 67P/C-G is clearly depleted in argon relative to solar, which can be accounted for by an ice trapping temperature that would not permit complete retention of argon or additional contributions of xenon (and krypton). Noble gas trapping in amorphous ice as a function of temperature is represented by the thin blue line and blue bars given by (24) based on data from (25). Taken at face value, 67P/C-G noble gas relative abundances would require relatively high trapping temperature (≥70 K), which is not consistent with other 67P/C-G coma measurements. For instance, the CO/N_2 ratio requires temperatures ≤50 K (26).

Relative abundances of volatile species in the coma of comet 67P/C-G are the result of their trapping efficiencies in the cometesimals, as well as release and diffusion throughout the porosity of cometary ices. Comet 67P/C-G belongs to the group of Jupiter-Family Comets (JFCs), which most likely spent most of their life in the scattered disk. These objects do not easily become JFCs but are thought to have undergone a series of gravitational scattering processes, which leave them for several million years as Centaurs at intermediate distances from the Sun (27), while comets from the Oort Cloud (OCC) have a very different dynamical history, and their trajectories differ significantly from those of JFCs.

The thermal evolution of comet 67P/C-G assuming 10 Ma in a Centaur orbit at 7 AU has been simulated (28). These simulations yield inhomogeneous temperatures up to 80 to 90 K inside the nucleus at a depth of at least a kilometer. In combination with the amorphous to crystalline transition or any kind of destabilization of ices, this leads to nonhomogeneous subsurface composition as an evolutionary process, even before the comet's first apparition in the inner solar system.

At these temperatures and over a time span of several million years, species of high volatility may partially diffuse from the comet and be lost (29). As a consequence, the abundance of highly volatile species may be altered in JFCs and different from OCCs, provided that the bulk outgassing occurs from an altered layer. The CO production rate of 67P/C-G around perihelion is ~1% compared to water. This is toward the low end of CO production rates compared to other comets, where production rates extend up to 25% (30). Comets are depleted in nitrogen by at least a factor of 5. This was explained by not incorporating the full complement of N_2 or by loss of N_2 during the lifetime of the comet (31). The low abundance of the highly volatile CO and N_2 (26) could have the same origin, namely, selective diffusion in amorphous ice. This would then also have led to loss of argon and, if initially present at all, neon.

The erosion of 67P/C-G is estimated to be a few tens of meters per pericenter passage (9). The comet has been in its current orbit since a close encounter with Jupiter in 1959, but even before that, it may have been inside of 5 AU for several centuries (32), and thus, several hundreds of meters of surface erosion could have significantly altered the size and shape of the comet. It may therefore have lost most of the layer affected by the heat wave during the Centaur stage, but this is difficult to assess.

Another possibility for the apparent mismatch of our results compared to amorphous ice laboratory measurements is the specific set of conditions (for example, gas composition and pressure) that are not representative of conditions in nature. The temperature of release of volatile species, in particular from amorphous ice, can be significantly different from their trapping temperature and depends on the ice in which they are embedded (33). Hence, Kouchi and Yamamoto (34) also investigated the trapping and release of gases in mixtures better representing the volatile species in a comet. In particular, the non-negligible

Fig. 4. Noble gas relative abundances compared to other solar system reservoirs. Sources of data: 67P/C-G: production rate ratios with 1-σ errors (SEM and calibration uncertainties) derived from Table 1, $^{84}Kr/^{36}Ar$ = 0.058 ± 0.013, and $^{132}Xe/^{36}Ar$ = 0.013 ± 0.003; solar: (18); Earth and Mars: (43); chondritic: CRPG compilation of CI and CM data; amorphous water ice: (24, 25). The blue arrow indicates the presumed composition of the initial atmosphere of Earth before secondary loss of xenon, and possibly krypton, to space through geological periods of time. The two red arrows represent upper limits for the $^{132}Xe/^{36}Ar$ and $^{84}Kr/^{36}Ar$ ratios measured in Titan by the Cassini-Huygens probe (23).

abundance of CO_2 influences the trapping and subsequent release of volatile species from amorphous ices. Parts of the CO_2 are embedded in the water ice, while also patches of CO_2 ice form. With a mixture of 65:10:10:15 of H_2O:CO_2:CH_4:CO, the very volatile species, CO and CH_4, trap much better and are released in a complicated pattern compared to mixtures with pure water ice only. The same behavior can be observed for argon and N_2 in mixtures of H_2O and CO_2, which raises the question on the (relative) trapping behavior of the other noble gases neon, krypton, and xenon (35). From mixtures of H_2O:Ne at different temperatures between 15 and 35 K, the Ne/H_2O ratio drops sharply already at 35 K to the value of 10^{-4} (36). The gas is released from the amorphous ice during the transformations to crystalline ice from 130 to 160 K. The estimated upper limit of 5×10^{-8} would rise the cometary ice formation temperature to 40 K. However, the release of krypton and xenon in 67P/C-G was detected from the southern, winter hemisphere very late in the mission. At this time in the mission, water sublimation from the south was more or less shut off, while CO_2 was still abundant (17). The abundant CO_2 relative to water suggests that these noble gases are predominantly trapped in the CO_2 fraction of the ice. This may also explain the poor correlation of argon with H_2O (10). The interpretation of our results requires more laboratory experiments, where trapping in more comet-like mixtures, with H_2O and at least CO_2, is investigated.

Similar to amorphous ice studies, the trapping and desorption capabilities of other ices like clathrate hydrates or polycrystalline ice must also be investigated in depth using appropriate gaseous mixtures. Many laboratory experiments, including species such as argon, krypton, and xenon, have been made in the 100 to 273 K range (37), but none of them are close to astrophysical conditions and compositions. Argon, krypton, and xenon abundances in clathrates formed in the protosolar nebula in the vicinity of the giant planets were predicted close to the observed values (38). However, the gaseous mixture used in this simulation is dominated by CO, which is not consistent with 67P/C-G observations where CO was much less abundant compared to H_2O and CO_2. In addition, pressure and temperature conditions were chosen to reflect average nebular conditions and might differ from the actual region where 67P/C-G formed. They also performed the same computation for a CH_4-dominated mixture, which yielded very different relative noble gas abundances. These experiments show that the results depend strongly on the major molecule(s) and on pressure and temperature. No trapping or release data for noble gases exist for polycrystalline ices. Hence, additional laboratory results that are based on appropriate mixtures are needed for a comparison with ROSINA's observations. This includes the investigation to determine whether simultaneous release of CO_2 and noble gases is compatible with clathrates. Another well-known issue with the growth of clathrates in low-pressure environments in the outer (trans-Neptunian) protosolar nebula is their very slow formation kinetics, which can take longer than the disk lifetime, and is mainly due to the lack of available "fresh" ice (38). A way to overcome this issue is to assume that collisions between ice grains during planetesimal formation produce fresh ice at their surface and ease the clathrate formation process.

Finally, the starting composition of the gas might not have been solar, as suggested by xenon isotopic measurements (12), and the comparison with amorphous ice data, which assume a solar-like initial gas, may not be fully relevant. The same has to be considered in future experiments using also other types of ice. We think that the problem is far from being solved and that the present measurement of cometary noble gases, which has never been done before, will motivate further experimental and theoretical studies.

The Earth and Mars data points in Fig. 4 are off mixing lines that join solar, chondritic, or cometary compositions. These trends were taken as evidence for a cometary contribution to Earth and Mars (39) based on amorphous ice measurements (25). Recently, however, the xenon depletion of the terrestrial atmosphere has been attributed to preferential loss of this gas to space during geological periods of time (40, 41) based on the observation that the isotopic composition of xenon in the Archean Eon was intermediate between the primordial and modern atmosphere's one (the modern terrestrial atmospheric xenon being isotopically fractionated relative to primordial xenon). A more limited fraction of krypton might also have been lost (modern atmospheric krypton is also fractionated but to a lesser extent than xenon). A similar process might have also acted on Mars as martian atmospheric xenon is also depleted and isotopically fractionated. Thus, the initial composition of the terrestrial atmosphere (and possibly of the martian one) was presumably shifted toward higher Xe/Ar and Kr/Ar values ("initial Earth," blue arrow in Fig. 4), which would place the data points closer to a mixing line between chondritic and cometary. When corrected for xenon atmospheric loss on Earth, the noble gas composition of the "restored" Earth would fall between the average chondritic and the cometary compositions in Fig. 4. This location suggests that the atmosphere received contributions from both cosmochemical sources. This possibility is in full agreement with the independent evidence based on xenon isotopes that comets contributed 22 ± 5% cometary xenon to a 78 ± 5% chondritic xenon atmosphere (12).

Figure 4 shows the upper limits of possible Kr/Ar and Xe/Ar ratios estimated in Titan's atmosphere from measurements by the gas chromatograph–mass spectrometer (GC-MS) aboard the Cassini-Huygens probe. Among the primordial noble gases, only ^{36}Ar has been firmly detected by the GC-MS with an atmospheric mole fraction of ~2.06×10^{-7} (23). On the other hand, only upper limits of 1×10^{-8} have been inferred for the atmospheric mole fractions of krypton and xenon (we assume that the reported upper limits correspond to the major isotopes ^{84}Kr and ^{132}Xe). Some of the noble gases could have been trapped in the forming aerosols in Titan's atmosphere, which settled on the surface, thus lowering the krypton and xenon below the detection limit (42). A comparison between the upper limits of Xe/Ar and Kr/Ar ratios in Titan and 67P/C-G shows that the ^{84}Kr/^{36}Ar ratio measured in the comet $(5.85 \pm 1.33) \times 10^{-2}$ overlaps within error bars with the upper limit (4.85×10^{-2}) measured in Titan. In addition, the upper limit of the ^{132}Xe/^{36}Ar ratio derived in Titan does not exclude 67P/C-G's value. Both, Titan and 67P/C-G, formed beyond the snowline in the protosolar nebula, and our data do not fully exclude a common origin for the building blocks from which both bodies agglomerated.

MATERIALS AND METHODS
ROSINA DFMS instrument
Neutral gas that entered the ion source was ionized by 45-eV electrons and subsequently accelerated into the analyzer section of the sensor. After a 90° deflection in an electrostatic analyzer and a 60° deflection in a permanent magnet, only ions with a very specific mass/charge can make it to the microchannel panel (MCP) detector (2). Ions impacting on the MCP trigger an avalanche of electrons, which are then collected and measured on a Linear Electron Detector Array (LEDA). For proper operation, an initial charge was applied to the LEDA that generates an offset that has to be subsequently removed (3, 14). The MCP/LEDA detector consists of two parallel arrays, row A and row B, for redundancy. Both rows contain 512 pixels each, which allow obtaining

one mass spectrum per row around a preset mass in one go without changing any of the voltages.

Any given mass/charge ratio requires a specific set of potentials to be applied, and a single measurement lasts approximately 30 s. After the voltages were set, which took roughly 10 s, the signal was accumulated for ~20 s. This process was then repeated mass after mass, and a nominal mass scan from mass/charge 13 to 100 u/e took roughly 45 min. Therefore, DFMS was operated in a dedicated noble gas mode in which only a subset of the whole mass range was measured (details shown in table S4). Given the sequential measurement of different masses, DFMS was set to adjust the detector gain voltage based on ion current on the detector. For weak signals, including all noble gases (argon, krypton, and xenon), the highest amplification was chosen automatically. However, H_2O, CO_2, and CO (governing the signal on the mass/charge 28 u/e channel with N_2) are more abundant, and therefore, the spectra were obtained at lower gain amplifications. The relative amplifications were calibrated in the laboratory, and corresponding factors (~2.63 amplification of the signal per gain step) were taken into account when computing relative abundances with respect to H_2O, CO_2, and N_2. Furthermore, we restricted our analysis of the relative abundances of ^{36}Ar to N_2 and N_2 to CO_2 to measurements that were obtained within a maximum difference of three gain steps.

Not all channels on the MCP receive the same signal intensity over time, which leads to nonuniform aging depending, to first order, on the accumulated lifetime charge of each channel. This was monitored at regular intervals by varying the voltages such that a water beam was moved across the whole detector. From the variation of the signal, the sensitivities of each channel can then be derived. For the isotopic measurements reported here, however, the individual isotopes were measured one after the other and fell more or less on the exact same pixels, which, to first order, removed any errors associated with the aging process of the individual pixels. Row B was more sensitive compared to row A, and we therefore focus on row B in this work.

For the data analysis, first, the LEDA offset due to the initially applied charge was removed. Afterward, the pixel gain due to the different aging of the individual MCP channels was corrected for. Furthermore, mass fractionation in the mass analyzer has to be corrected for: In DFMS, the heavier species require a lower energy to make it through the analyzer section. Hence, also the impact velocity and thus yield at the MCP detector are lower. The correction was obtained from the laboratory calibration campaign.

The in-flight gas calibration unit flown together with the flight model of DFMS contained gases of neon, CO_2, and xenon. Therefore, the different noble gases (neon, argon, krypton, and xenon), together with other cometary volatile species including H_2O, CO_2, and N_2, which are discussed in this paper, were calibrated using the flight spare instrument in the laboratory. DFMS instrument sensitivities relate the abundances of the corresponding species inside the ion source to the measured signal of the MCP/LEDA detector used here. They were derived through cross-calibration using a reference Granville-Phillips Series 370 Stabil-Ion gauge at different pressures of the compound in question. Details on the calibration and the values can be found in the NASA Planetary Data System (PDS) and ESA Planetary Science Archive (PSA) archives (see the "Data and materials availability" section under Acknowledgments).

Statistical errors
The statistical count error of the average counts per spectrum (for example, $\Delta^{80}Kr_{counts}$) is obtained from the square root of the average counts per spectrum (for example, $\Delta^{80}Kr$) divided by the number of

spectra, $\Delta^{80}Kr_{counts} = \sqrt{^{80}Kr/N_{spectra}}$. Then follows a systematic error of the offset subtraction based on the peak width in number of pixels and the uncertainty of the offset per pixel, for example, $\Delta^{80}Kr_{offset} = N_{pixel} \times \Delta offset$. In the special case of ^{80}Kr follows the estimated error of 60% due to the strong interference of $C^{34}S_2$, which is close in mass and cannot be fully resolved by DFMS, and the same is true for $H^{79}Br$ (15), $\Delta^{80}Kr_{fit} = 0.6 \times {}^{80}Kr$. Therefore, uncertainties for ^{80}Kr are too large for any meaningful contribution to our analysis. The total error for the average counts is obtained from the square root of the sum of the squared individual errors, $\Delta^{80}Kr = \sqrt{\Delta^{80}Kr_{counts}^2 + \Delta^{80}Kr_{offset}^2 + \Delta^{80}Kr_{fit}^2}$.

Finally, the errors after normalization to ^{84}Kr are obtained by error propagation, for example

$$\Delta\left(\frac{^{80}Kr}{^{84}Kr}\right) = \sqrt{\left(\frac{1}{^{84}Kr}\right)^2 (\Delta^{84}Kr)^2 + \left(\frac{^{80}Kr}{(^{84}Kr)^2}\right)^2 (\Delta^{84}Kr)^2}$$

For argon, corresponding errors are obtained through error propagation, that is, for $^{36}Ar/^{38}Ar = r \pm \Delta r = 5.4 \pm 1.4$ (10) follows

$$^{36}Ar/Ar = r/(r+1) = 5.4/(5.4+1.0) = 0.844$$

and

$$\Delta(^{36}Ar/Ar) = \frac{\Delta r}{(r+1)^2} = 0.034$$

More details and an example for xenon can be found in the Supplementary Materials of (12). The errors of the relative abundances between the different noble gases and between the noble gases and H_2O, CO_2, or N_2 were computed accordingly.

Mixing model
We modeled the isotopic compositions of 67P/C-G krypton and xenon as the result of mixing between an exotic component rich in s-process isotopes and labeled here as X with a normal component resembling solar noble gases, for example, the N-component identified in presolar material [see (20, 22) and the Discussion section for justification and (11) for summary of data]. For one isotope j of xenon, ^jXe, the mass balance equation is

$$^jXe_O = {}^jXe_X + {}^jXe_N \qquad (1)$$

where suffixes O, X, and N refer to cometary, exotic, and normal, respectively. Let α be the fraction of exotic ^jXe_X in cometary ^jXe_O

$$\alpha = \frac{^jXe_X}{^jXe_O} \qquad (2)$$

We also have

$$\frac{^jXe_N}{^jXe_X} = \frac{1-\alpha}{\alpha} \qquad (3)$$

Let us consider another isotope j of xenon, the isotopic ratio ${}^i R = {}^i Xe/{}^j Xe$ is

$$
{}^i R_O = \alpha \, {}^i R_X + (1 - \alpha) \, {}^i R_N \tag{4}
$$

with α defined in Eq. 2 as the fraction of the denominator isotope (here ${}^{132}Xe$) in X relative to O. A similar equation can be written for krypton

$$
{}^j Kr_O = {}^j Kr_X + {}^j Kr_N \tag{5}
$$

$$
\beta = \frac{{}^j Kr_X}{{}^j Kr_O} \tag{6}
$$

$$
\frac{{}^j Kr_N}{{}^j Kr_X} = \frac{1 - \beta}{\beta} \tag{7}
$$

Let us consider the Xe/Kr ratio. The mixing equation can be written as

$$
\left(\frac{Xe}{Kr} \right)_O = \frac{ \left(\frac{Xe}{Kr} \right)_X + \left(\frac{Xe}{Kr} \right)_N \left(\frac{Kr_N}{Kr_X} \right) }{ 1 + \left(\frac{Kr_N}{Kr_X} \right) } \tag{8}
$$

which can be rewritten as

$$
\left(\frac{Xe}{Kr} \right)_X = \frac{ \left(\frac{Xe}{Kr} \right)_O - (1 - \beta) \left(\frac{Xe}{Kr} \right)_N }{ \beta } \tag{9}
$$

This equation gives the Xe/Kr ratio of the exotic component required to yield the Xe/Kr ratio of the comet. In the following, the Xe/Kr ratios were normalized to the solar value. The normalized cometary ratio is 5, (main text) and let us assume that the normal component has a solar-like ratio $[(Xe/Kr)_N = 1]$. For krypton, the best isotopic fit was obtained for $\beta = 0.05$ (main text and Fig. 1). It comes out that the exotic component should have a $(Xe/Kr)_X$ ratio of 81 to fit the mixing equation, very rich indeed in xenon relative to krypton and solar.

We can also compute the fraction of Xe_N to cometary Xe_O for a $(Xe/Kr)_X$ ratio of 81. Eq. 9 can be rewritten as

$$
\left(\frac{Kr}{Xe} \right)_O = \frac{ \left(\frac{Kr}{Xe} \right)_X + \left(\frac{Kr}{Xe} \right)_N \left(\frac{Xe_N}{Xe_X} \right) }{ 1 + \left(\frac{Xe_N}{Xe_X} \right) } \tag{10}
$$

which can be rearranged as

$$
\left(\frac{Xe_N}{Xe_X} \right) = \frac{ \left(\frac{Kr}{Xe} \right)_X - \left(\frac{Kr}{Xe} \right)_O }{ \left(\frac{Kr}{Xe} \right)_O - \left(\frac{Kr}{Xe} \right)_N } \tag{11}
$$

which gives 0.234. The fraction of exotic xenon in cometary xenon, defined as α in Eq. 2 and computed using Eq. 3, is 0.81, which is identical to the fraction of 0.8 obtained to fit best the xenon isotopic data (fig. S5). Thus, two different approaches yield consistent results, giving strength to the mixing model developed in this contribution.

SUPPLEMENTARY MATERIALS

Supplementary material for this article is available at http://advances.sciencemag.org/cgi/content/full/4/7/eaar6297/DC1

Fig. S1. Averaged ROSINA DFMS mass spectra containing the major krypton isotopes.
Fig. S2. Observation geometry for the noble gas observations in May 2016.
Fig. S3. Observation geometry before perihelion in May 2015 and early June 2015 used to derive the N_2/H_2O ratio.
Fig. S4. N_2 versus H_2O abundances for before perihelion in May 2015 and early June 2015.
Fig. S5. Mix of exotic X-Xe with normal N-Xe compared to 67P/C-G xenon.
Table S1. Krypton average counts per spectrum (~20-s integration time) including errors and below the associated isotopic ratios with respect to ${}^{84}Kr$ with errors for the three periods.
Table S2. Ratio of ${}^{36}Ar$ to total argon, ${}^{84}Kr$ to total krypton, and ${}^{132}Xe$ to total xenon.
Table S3. Bulk abundances of noble gases in the coma of comet 67P/C-G.
Table S4. Measured mass/charge ratios in the dedicated noble gas mode.

REFERENCES AND NOTES

1. K.-H. Glassmeier, H. Boehnhardt, D. Koschny, E. Kührt, I. Richter, The ROSETTA Mission: Flying towards the origin of the solar system. *Space Sci. Rev.* **128**, 1–21 (2007).
2. H. Balsiger, K. Altwegg, P. Bochsler, P. Eberhardt, J. Fischer, S. Graf, A. Jäckel, E. Kopp, U. Langer, M. Mildner, J. Müller, T. Riesen, M. Rubin, S. Scherer, P. Wurz, S. Wüthrich, E. Arijs, S. Delanoye, J. De Keyser, E. Neefs, D. Nevejans, H. Rème, C. Aoustin, C. Mazelle, J.-L. Médale, J. A. Sauvaud, J.-J. Berthelier, J.-L. Bertaux, L. Duvet, J.-M. Illiano, S. A. Fuselier, A. G. Ghielmetti, T. Magoncelli, E. G. Shelley, A. Korth, K. Heerlein, H. Lauche, S. Livi, A. Loose, U. Mall, B. Wilken, F. Gliem, B. Fiethe, T. I. Gombosi, B. Block, G. R. Carignan, L. A. Fisk, J. H. Waite, D. T. Young, H. Wollnik, Rosina—Rosetta Orbiter Spectrometer for Ion and Neutral Analysis. *Space Sci. Rev.* **128**, 745–801 (2007).
3. L. Le Roy, K. Altwegg, H. Balsiger, J.-J. Berthelier, A. Bieler, C. Briois, U. Calmonte, M. R. Combi, J. De Keyser, F. Dhooghe, B. Fiethe, S. A. Fuselier, S. Gasc, T. I. Gombosi, M. Hässig, A. Jäckel, M. Rubin, C.-Y. Tzou, Inventory of the volatiles on comet 67P/Churyumov-Gerasimenko from Rosetta/ROSINA. *Astron. Astrophys.* **583**, A1 (2015).
4. A. Bieler, K. Altwegg, H. Balsiger, A. Bar-Nun, J. J. Berthelier, P. Bochsler, C. Briois, U. Calmonte, M. Combi, J. De Keyser, E. F. van Dishoeck, B. Fiethe, S. A. Fuselier, S. Gasc, T. I. Gombosi, K. C. Hansen, M. Hässig, A. Jäckel, E. Kopp, A. Korth, L. Le Roy, U. Mall, R. Maggiolo, B. Marty, O. Mousis, T. Owen, H. Rème, M. Rubin, T. Sémon, C. Y. Tzou, J. H. Waite, C. Walsh, P. Wurz, Abundant molecular oxygen in the coma of comet 67P/Churyumov-Gerasimenko. *Nature* **526**, 678–681 (2015).
5. M. Hässig, K. Altwegg, H. Balsiger, A. Bar-Nun, J. J. Berthelier, A. Bieler, P. Bochsler, C. Briois, U. Calmonte, M. Combi, J. De Keyser, P. Eberhardt, B. Fiethe, S. A. Fuselier, M. Galand, S. Gasc, T. I. Gombosi, K. C. Hansen, A. Jäckel, H. U. Keller, E. Kopp, A. Korth, E. Kührt, L. Le Roy, U. Mall, B. Marty, O. Mousis, E. Neefs, T. Owen, H. Rème, M. Rubin, T. Sémon, C. Tornow, C. Y. Tzou, J. H. Waite, P. Wurz, Time variability and heterogeneity in the coma of 67P/Churyumov-Gerasimenko. *Science* **347**, aaa0276 (2015).
6. N. Fougere, K. Altwegg, J.-J. Berthelier, A. Bieler, D. Bockelée-Morvan, U. Calmonte, F. Capaccioni, M. R. Combi, J. De Keyser, V. Debout, S. Erard, B. Fiethe, G. Filacchione, U. Fink, S. A. Fuselier, T. I. Gombosi, K. C. Hansen, M. Hässig, Z. Huang, L. Le Roy, C. Leyrat, A. Migliorini, G. Piccioni, G. Rinaldi, M. Rubin, Y. Shou, V. Tenishev, G. Toth, C.-Y. Tzou; ROSINA Teams, Direct simulation Monte Carlo modelling of the major species in the coma of comet 67P/Churyumov-Gerasimenko. *Mon. Not. R. Astron. Soc.* **462**, S156–S169 (2016).
7. J. De Keyser, F. Dhooghe, K. Altwegg, H. Balsiger, J.-J. Berthelier, C. Briois, U. Calmonte, G. Cessateur, M. R. Combi, E. Equeter, B. Fiethe, S. Fuselier, S. Gasc, A. Gibbons, T. Gombosi, H. Gunell, M. Hässig, L. Le Roy, R. Maggiolo, U. Mall, B. Marty, E. Neefs, H. Rème, M. Rubin, T. Sémon, C.-Y. Tzou, P. Wurz, Evidence for distributed gas sources of hydrogen halides in the coma of comet 67P/Churyumov–Gerasimenko. *Mon. Not. R. Astron. Soc.* **469**, S695–S711 (2017).
8. H. U. Keller, S. Mottola, S. F. Hviid, J. Agarwal, E. Kührt, Y. Skorov, K. Otto, J.-B. Vincent, N. Oklay, S. E. Schröder, B. Davidsson, M. Pajola, X. Shi, D. Bodewits, I. Toth, F. Preusker, F. Scholten, H. Sierks, C. Barbieri, P. Lamy, R. Rodrigo, D. Koschny, H. Rickman, M. F. A'Hearn, M. A. Barucci, J.-L. Bertaux, I. Bertini, G. Cremonese, V. Da Deppo, S. Debei, M. De Cecco, J. Deller, S. Fornasier, M. Fulle, O. Groussin, P. J. Gutiérrez, C. Güttler, M. Hofmann, W.-H. Ip, L. Jorda, J. Knollenberg, J. R. Kramm, M. Küppers, L.-M. Lara, M. Lazzarin, J. J. Lopez-Moreno, F. Marzari, G. Naletto, C. Tubiana, N. Thomas, Seasonal mass transfer on the nucleus of comet 67P/Chuyumov–Gerasimenko. *Mon. Not. R. Astron. Soc.* **469**, S357–S371 (2017).
9. H. U. Keller, S. Mottola, B. Davidsson, S. E. Schröder, Y. Skorov, E. Kührt, O. Groussin, M. Pajola, S. F. Hviid, F. Preusker, F. Scholten, M. F. A'Hearn, H. Sierks, C. Barbieri, P. Lamy, R. Rodrigo, D. Koschny, H. Rickman, M. A. Barucci, J.-L. Bertaux, I. Bertini, G. Cremonese, V. Da Deppo, S. Debei, M. De Cecco, S. Fornasier, M. Fulle, P. J. Gutiérrez, W.-H. Ip, L. Jorda, J. Knollenberg, J. R. Kramm, M. Küppers, L. M. Lara, M. Lazzarin, J. J. Lopez Moreno, F. Marzari, H. Michalik, G. Naletto, L. Sabau, N. Thomas, J.-B. Vincent, K.-P. Wenzel,

J. Agarwal, C. Güttler, N. Oklay, C. Tubiana, Insolation, erosion, and morphology of comet 67P/Churyumov-Gerasimenko. *Astron. Astrophys.* **583**, A34 (16) (2015).

10. H. Balsiger, K. Altwegg, A. Bar-Nun, J. J. Berthelier, A. Bieler, P. Bochsler, C. Briois, U. Calmonte, M. Combi, J. De Keyser, P. Eberhardt, B. Fiethe, S. A. Fuselier, S. Gasc, T. I. Gombosi, K. C. Hansen, M. Hässig, A. Jäckel, E. Kopp, A. Korth, U. Le Roy, U. Mall, B. Marty, O. Mousis, T. Owen, H. Rème, M. Rubin, T. Sémon, C. Y. Tzou, J. H. Waite, P. Wurz, Detection of argon in the coma of comet 67P/Churyumov-Gerasimenko. *Sci. Adv.* **1**, e1500377 (2015).

11. U. Ott, Planetary and pre-solar noble gases in meteorites. *Chem. Erde-Geochem.* **74**, 519–544 (2014).

12. B. Marty, K. Altwegg, H. Balsiger, A. Bar-Nun, D. V. Bekaert, J. J. Berthelier, A. Bieler, C. Briois, U. Calmonte, M. Combi, J. De Keyser, B. Fiethe, S. A. Fuselier, S. Gasc, T. I. Gombosi, K. C. Hansen, M. Hässig, A. Jäckel, E. Kopp, A. Korth, L. Le Roy, U. Mall, O. Mousis, T. Owen, H. Rème, M. Rubin, T. Sémon, C. Y. Tzou, J. H. Waite, P. Wurz, Xenon isotopes in 67P/Churyumov-Gerasimenko show that comets contributed to Earth's atmosphere. *Science* **356**, 1069–1072 (2017).

13. K. Lodders, H. Palme, H. P. Gail, Solar system abundances of the elements, in *Principles and Perspectives in Cosmochemistry*, A. Goswami, B. E. Reddy, Eds. (Springer, 2010), pp. 379–417.

14. U. Calmonte, K. Altwegg, H. Balsiger, J. J. Berthelier, A. Bieler, G. Cessateur, F. Dhooghe, E. F. van Dishoeck, B. Fiethe, S. A. Fuselier, S. Gasc, T. I. Gombosi, M. Hässig, L. Le Roy, M. Rubin, T. Sémon, C.-Y. Tzou, S. F. Wampfler, Sulphur-bearing species in the coma of comet 67P/Churyumov–Gerasimenko. *Mon. Not. R. Astron. Soc.* **462**, S253–S273 (2016).

15. F. Dhooghe, J. De Keyser, K. Altwegg, C. Briois, H. Balsiger, J.-J. Berthelier, U. Calmonte, G. Cessateur, M. R. Combi, E. Equeter, B. Fiethe, N. Fray, S. Fuselier, S. Gasc, A. Gibbons, T. Gombosi, H. Gunell, M. Hässig, M. Hilchenbach, L. Le Roy, R. Maggiolo, U. Mall, B. Marty, E. Neefs, H. Rème, M. Rubin, T. Sémon, C.-Y. Tzou, P. Wurz, Halogens as tracers of protosolar nebula material in comet 67P/Churyumov-Gerasimenko. *Mon. Not. R. Astron. Soc.* **472**, 1336–1345 (2017).

16. V. Tenishev, M. Combi, B. Davidsson, A global kinetic model for cometary comae: The evolution of the coma of the *Rosetta* target comet churyumov-gerasimenko throughout the mission. *Astrophys. J.* **685**, 659–677 (2008).

17. S. Gasc, K. Altwegg, H. Balsiger, J.-J. Berthelier, A. Bieler, U. Calmonte, B. Fiethe, S. Fuselier, A. Galli, T. Gombosi, M. Hoang, J. De Keyser, A. Korth, L. Le Roy, U. Mall, H. Rème, M. Rubin, T. Sémon, C.-Y. Tzou, J. H. Waite, P. Wurz, Change of outgassing pattern of 67P/Churyumov–Gerasimenko during the March 2016 equinox as seen by ROSINA. *Mon. Not. R. Astron. Soc.* **469**, S108–S117 (2017).

18. A. Meshik, C. Hohenberg, O. Pravdivtseva, D. Burnett, Heavy noble gases in solar wind delivered by Genesis mission. *Geochim. Cosmochim. Acta* **127**, 326–347 (2014).

19. J. D. Gilmour, G. Turner, Constraints on nucleosynthesis from xenon isotopes in presolar material. *Astrophys. J. Lett.* **657**, 600 (2007).

20. R. S. Lewis, S. Amari, E. Anders, Interstellar grains in meteorites: II. SiC and its noble gases. *Geochim. Cosmochim. Acta* **58**, 471–494 (1994).

21. R. Gallino, M. Busso, G. Picchio, C. M. Raiteri, On the astrophysical interpretation of isotope anomalies in meteoritic SiC grains. *Nature* **348**, 298–302 (1990).

22. J. D. Gilmour, "Planetary" noble gas components and the nucleosynthetic history of solar system material. *Geochim. Cosmochim. Acta* **74**, 380–393 (2010).

23. H. B. Niemann, S. K. Atreya, J. E. Demick, D. Gautier, J. A. Haberman, D. N. Harpold, W. T. Kasprzak, J. I. Lunine, T. C. Owen, F. Raulin, Composition of Titan's lower atmosphere and simple surface volatiles as measured by the Cassini-Huygens probe gas chromatograph mass spectrometer experiment. *J. Geophys. Res.* **115**, n/a–n/a (2010).

24. N. Dauphas, The dual origin of the terrestrial atmosphere. *Icarus* **165**, 326–339 (2003).

25. A. Bar-Nun, I. Kleinfeld, E. Kochavi, Trapping of gas mixtures by amorphous water ice. *Phys. Rev. B* **38**, 7749–7754 (1988).

26. M. Rubin, K. Altwegg, H. Balsiger, A. Bar-Nun, J.-J. Berthelier, A. Bieler, P. Bochsler, C. Briois, U. Calmonte, M. Combi, J. De Keyser, F. Dhooghe, P. Eberhardt, B. Fiethe, S. A. Fuselier, S. Gasc, T. I. Gombosi, K. C. Hansen, M. Hässig, A. Jäckel, E. Kopp, A. Korth, L. Le Roy, U. Mall, B. Marty, O. Mousis, T. Owen, H. Rème, T. Sémon, C.-Y. Tzou, J. H. Waite, P. Wurz, Molecular nitrogen in comet 67P/Churyumov-Gerasimenko indicates a low formation temperature. *Science* **348**, 232–235 (2015).

27. J. Horner, N. W. Evans, M. E. Bailey, Simulations of the population of Centaurs—I. The bulk statistics. *Mon. Not. R. Astron. Soc.* **354**, 798–810 (2004).

28. A. Guilbert-Lepoutre, E. D. Rosenberg, D. Prialnik, S. Besse, Modelling the evolution of a comet subsurface: Implications for 67P/Churyumov–Gerasimenko. *Mon. Not. R. Astron. Soc.* **462**, S146–S155 (2016).

29. T. Lauck, L. Karssemeijer, K. Shulenberger, M. Rajappan, K. I. Öberg, H. M. Cuppen, CO diffusion into amorphous H_2O Ices. *Astrophys. J. Lett.* **801**, 118 (2015).

30. M. J. Mumma, S. B. Charnley, The chemical composition of comets—Emerging taxonomies and natal heritage. *Annu. Rev. Astron. Astrophys* **49**, 471–524 (2011).

31. J. Geiss, Composition in Halley's Comet: Clues to origin and history of cometary matter, in *Cosmic Chemistry* (Springer, 1988), pp. 1–27.

32. M. Królikowska, 67P/Churyumov-Gerasimenko—Potential target for the Rosetta mission. *Acta Astron.* **53**, 195–209 (2003).

33. M. P. Collings, M. A. Anderson, R. Chen, J. W. Dever, S. Viti, D. A. Williams, M. R. S. McCoustra, A laboratory survey of the thermal desorption of astrophysically relevant molecules. *Mon. Not. R. Astron. Soc.* **354**, 1133–1140 (2004).

34. A. Kouchi, T. Yamamoto, Cosmoglaciology: Evolution of ice in interstellar space and the early solar system. *Prog. Cryst. Growth Charact. Mater.* **30**, 83–107 (1995).

35. A. N. Greenberg, D. Laufer, A. Bar-Nun, The effect of CO_2 on gases trapping in cometary ices. *Mon. Not. R. Astron. Soc.* **469**, S517–S521 (2017).

36. A. Bar-Nun, D. Laufer, O. Rebolledo, S. Malyk, H. Reisler, C. Wittig, , Gas trapping in ice and its release upon warming, in *The Science of Solar System Ices*, M. S. Gudipati, J. Castillo-Rogez, Eds. (Springer Science and Business Media, 2012), vol. 356.

37. D. E. Sloan, C. Koh, *Clathrate Hydrates of Natural Gases* (CRC/Taylor and Francis, ed. 3, 2007).

38. J. I. Lunine, D. J. Stevenson, Thermodynamics of clathrate hydrate at low and high-pressures with application to the outer solar-system. *Astrophys. J.* **58**, 493–531 (1985).

39. T. Owen, A. Bar-Nun, I. Kleinfeld, Possible cometary origin of heavy noble gases in the atmospheres of Venus, Earth and Mars. *Nature* **358**, 43–46 (1992).

40. M. Pujol, B. Marty, R. Burgess, Chondritic-like xenon trapped in Archean rocks: A possible signature of the ancient atmosphere. *Earth Planet. Sci. Lett.* **308**, 298–306 (2011).

41. G. Avice, B. Marty, R. Burgess, The origin and degassing history of the Earth's atmosphere revealed by Archean xenon. *Nat. Commun.* **8**, 15455 (2017).

42. R. Jacovi, A. Bar-Nun, Removal of Titan's noble gases by their trapping in its haze. *Icarus* **196**, 302–304 (2008).

43. M. Ozima, F. A. Podosek, *Noble Gas Geochemistry* (Cambridge Univ. Press, 2002).

Science Advances

Krypton isotopes and noble gas abundances in the coma of comet 67P/Churyumov-Gerasimenko

Martin Rubin, Kathrin Altwegg, Hans Balsiger, Akiva Bar-Nun, Jean-Jacques Berthelier, Christelle Briois, Ursina Calmonte, Michael Combi, Johan De Keyser, Björn Fiethe, Stephen A. Fuselier, Sebastien Gasc, Tamas I. Gombosi, Kenneth C. Hansen, Ernest Kopp, Axel Korth, Diana Laufer, Léna Le Roy, Urs Mall, Bernard Marty, Olivier Mousis, Tobias Owen, Henri Rème, Thierry Sémon, Chia-Yu Tzou, Jack H. Waite and Peter Wurz

ARTICLE TOOLS	http://advances.sciencemag.org/content/4/7/eaar6297
SUPPLEMENTARY MATERIALS	http://advances.sciencemag.org/content/suppl/2018/07/02/4.7.eaar6297.DC1
REFERENCES	This article cites 38 articles, 4 of which you can access for free http://advances.sciencemag.org/content/4/7/eaar6297#BIBL
PERMISSIONS	http://www.sciencemag.org/help/reprints-and-permissions

Use of this article is subject to the Terms of Service